

Article

# Copper Mineralization Potential of Late Triassic Granitoids in Northern Yidun Arc, SW China

Xing-Yuan Li <sup>1,2,\*</sup>, Jing-Ru Zhang <sup>3</sup>, Hao Song <sup>2,\*</sup> and Chun-Kit Lai <sup>4,5</sup> <sup>1</sup> School of Geography and Planning, Sun Yat-sen University, Guangzhou 510275, China<sup>2</sup> Department of Geology, University of Regina, Regina, SK S4S 0A2, Canada<sup>3</sup> Guangdong Province Academic of Environmental Science, Guangzhou 510045, China; zhangjrgucas@163.com<sup>4</sup> Faculty of Science, Universiti Brunei Darussalam, Gadong BE1410, Brunei; chunkit.lai@ubd.edu.bn<sup>5</sup> Centre of Excellence in Ore Deposits (CODES), University of Tasmania, Tasmania 7001, Australia

\* Correspondence: lixingyuan@mail.sysu.edu.cn (X.-Y.L.); songhao2014@cdut.edu.cn (H.S.);

Tel.: +86-020-8411-2307 (X.-Y.L.)

Received: 9 May 2019; Accepted: 27 May 2019; Published: 1 June 2019



**Abstract:** Yidun arc is an important constituent of the Sanjiang Tethyan Domain in SW China. The Changdagou pluton, located in the northern part of the Yidun Arc, mainly consists of granodiorite. In this study, we conducted in-situ LA-ICP-MS zircon U-Pb dating, and trace element and Hf isotope analyses on the Changdagou granites. Age dating results yielded a weighted mean U-Pb age of  $214.97 \pm 0.98$  Ma (MSWD = 1.2,  $2\sigma$ ), broadly coeval with extensive late Triassic magmatism across the Yidun Arc. All zircon grains analyzed showed high concentrations of Th, U, and HREE, with positive Ce and negative Eu anomalies.  $\log f_{O_2}$  and  $Ce_N/Ce_N^*$  values vary from FMQ  $-3.14$  to FMQ  $+7.44$  (average FMQ  $+3.98$ ), and 14 to 172 (avg. 98), respectively. The zircon  $Eu_N/Eu_N^*$  (avg. 0.22) ratios have no clear correlation with the  $Ce_N/Ce_N^*$  ratios, suggesting that the former were mainly affected by the magma water content. In addition, zircon  $\epsilon Hf(t)$  values vary in a narrow range ( $-2.9$  to  $-4.9$ , avg.  $-3.4$ ) that clusters around zero, indicating a greater component of mantle-derived magma. Hence, we propose that the Changdagou granodiorite was derived from a highly oxidized, “wet”, Cu-rich source, of the type likely to generate porphyry Cu mineralization. However, these parameters ( $\log f_{O_2}$ ,  $Eu_N/Eu_N^*$ ,  $(Ce/Nd)/Y$ , and  $\epsilon Hf(t)$ ) are all lower than those of intrusions associated with Cu ores at Pulang and Lannitang, which may explain why the Cu deposit discovered at Changdagou is small by comparison. Furthermore, on the basis of the decreasing trends of  $\epsilon Hf$ ,  $\log f_{O_2}$ , and  $H_2O$  content from south to north along the Yidun arc, we infer that the northern segment of the Yidun arc (including Changdagou) was located further away from the subduction front.

**Keywords:** Yidun arc; Changdagou granite; porphyry Cu deposits; paleotethys; zircon chemistry and isotopes

## 1. Introduction

The Sanjiang Tethyan Domain in the southeastern Tibet Plateau comprises various (micro)-continental blocks, volcanic arcs, and ophiolitic belts that were formed during the opening and closure of the Paleo-Tethys (Figure 1) [1]. The NNW-trending Yidun structure is the largest island arc preserved in the domain [2–4], and a number of important porphyry copper deposits (PCDs) were found in its southern section, such as the Pulang, Lannitang and Xuejiping. These PCDs were mainly formed in the Late Triassic (208–235 Ma) during the Indosinian Orogeny [5–7]. In contrast, only a few PCDs have been discovered in the northern section of the arc, with the Changdagou PCD being the largest one [8]. This raises questions on whether the paucity of PCD discovery is an issue of exploration work, deposit preservation, or a combination of these factors.

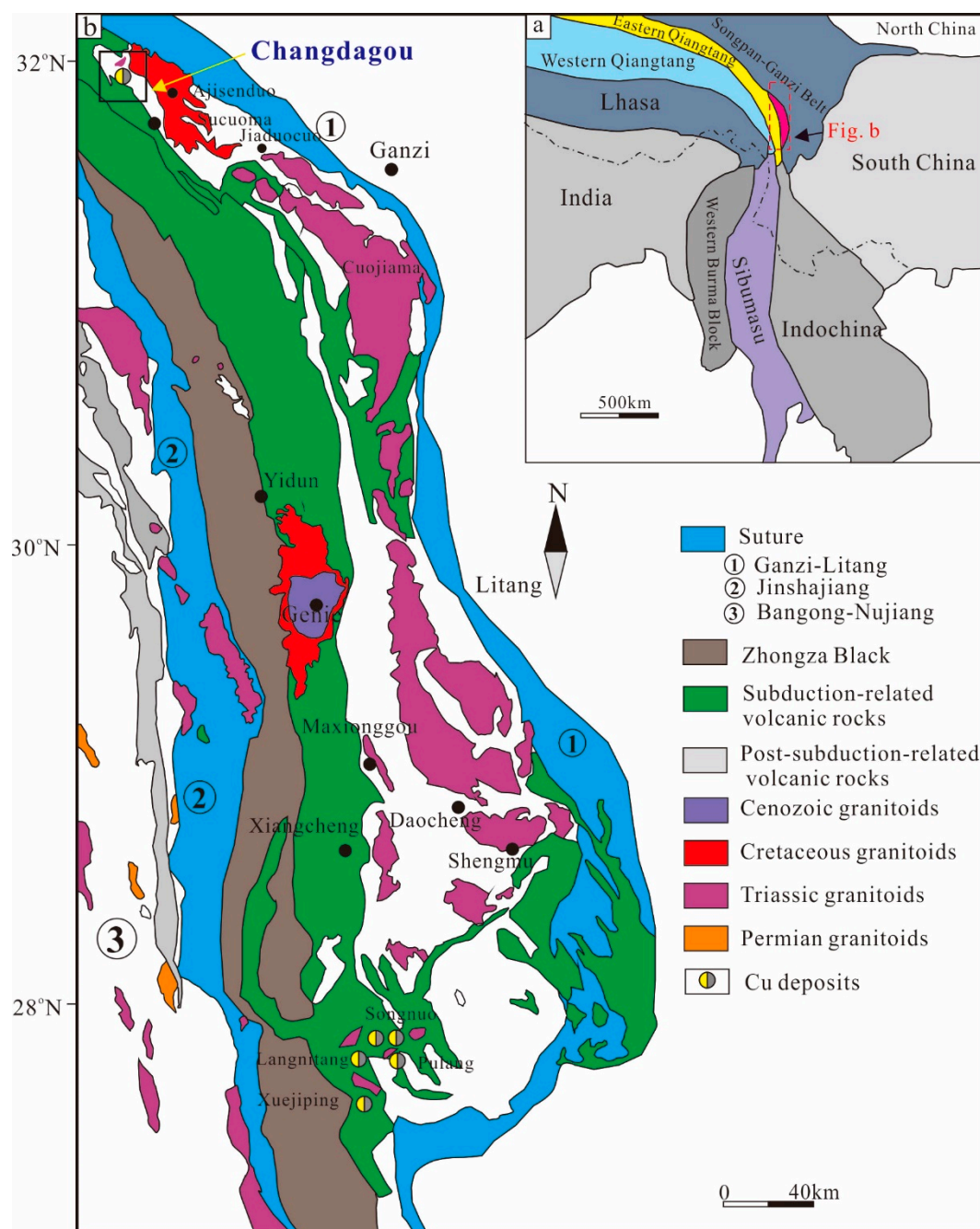


**Figure 1.** (a) Tectonic framework and distribution of major geological terranes and sutures of mainland SE Asia; (b) Tectonic framework of the Sanjiang Region, including the major geological terranes, sutures, volcanic rocks and intrusions (modified after [6]).

Redox state and water content of magmas are widely believed to be contributing factors for the formation of PCDs. Recent studies [9–14] revealed that zircon grain composition is sensitive to these factors, and can serve as an indicator of the magma physicochemical conditions. Ballard et al. [15] suggest PCDs are associated with zircon  $Ce^{4+}/Ce^{3+} > 300$  of magma, whilst Dilles [12] suggest that PCD fertile magmas commonly have  $Eu_N/Eu_N^* > 0.3$ . More recently, Lu et al. [14] argue that zircon trace element ratios, such as  $Eu_N/Eu_N^*$ ,  $Dy/Yb$ , and  $(Eu_N/Eu_N^*)/Y$ , can serve as proxies for the water content in magma. In addition, Hf isotopic signatures ( $\epsilon Hf$ ) can indicate whether the magma source was juvenile (with higher  $\epsilon Hf$ , i.e., close to the mantle value and enriched in radiogenic  $^{176}Hf$ ) or from an evolved, typically ancient crustal source (with lower  $\epsilon Hf$ ; [16–18]).

In this paper, we present a new zircon U-Pb age, trace element chemical and Hf isotope data on the Changdagou granodiorite porphyry in the northern Yidun arc. We discuss the redox state, water content, and possible magmatic source of the Changdagou granites, and compare these parameters with those in the Lannitang and Pulang granites in the southern Yidun arc. We evaluate some differences in mineralization potential between the northern and southern sections of the Yidun arc.

## 2. Geological Background

The Yidun arc and its PCDs have been described in many publications [1,16,19]. In brief, the Yidun arc is located between the Jinshajiang and Ganzi-Litang Paleo-Tethyan suture zones [2,20,21]. During the Late Triassic, closure of the Ganzi-Litang ocean basin might have led to the accretion of the Zhongza terrane onto the Yangtze craton via the Yidun arc [22] (Figure 1). It has been suggested that the Yidun arc was developed on the basement with the Yangtze craton inheritance [4,6,19], and underwent two magmatic episodes in the Late Triassic (218–230 Ma) and Late Cretaceous (88–105 Ma), responding the Paleo-Tethyan subduction and subsequent continent–continent collision (Figure 1a). The subduction-related magmatism formed several large granodioritic-granitic batholiths (e.g., Changdagou, Shengmu, Cuojaoma and Daocheng) in the northern Yidun arc [16,22], and dioritic-granitic stocks (e.g., Pulang and Lannitang) in the southern Yidun arc (also called the Zhongdian arc) [11,23–25].

The Changdagou PCD (~35 km from Dege city) is located in the northern Yidun arc, and contains ~76 kt Cu reserve [8]. The Changdagou intrusive complex intruded the black-gray slate and sandstone of the Upper Triassic Lanashan Formation (Figure 2). The intrusive complex comprises mainly granodiorite porphyry and minor quartz diorite porphyry stocks, and Changdagou PCD is closely related to the granodiorite porphyry. In this study, one granodiorite porphyry sample was collected from drill cores, which contain quartz (10–15%), plagioclase (25–55%), K-feldspar (10–30%) and biotite (3–5%), with accessory titanite, apatite, pyrite, and magnetite.

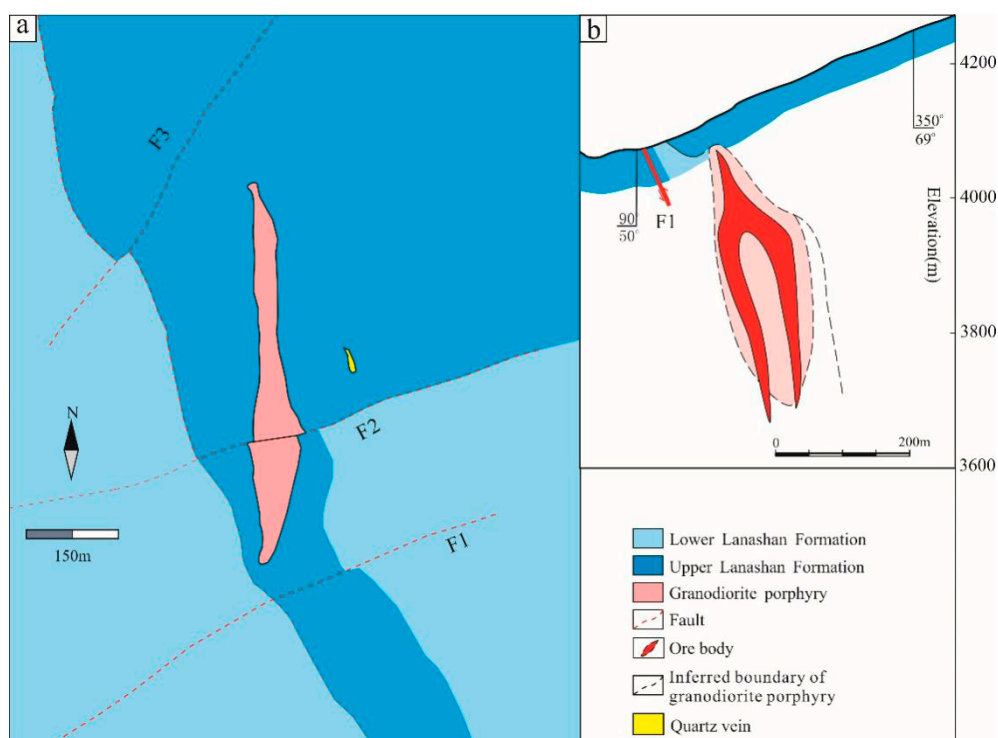


**Figure 2.** (a) Simplified geologic map of the Changdagou deposit (modified from [6]). (b) Geological profile for prospecting line No. 12.

Major alteration types in the Changdagou granite are silicic, potassic, sericite, argillic (kaolinite) and propylitic. Silicification occurs mainly in the ore-forming granodiorite and the silicified rocks in its exo-contact, and the orebody in the silicified zone is of higher grade. Quartz-calcite veins intersect each other in a grid pattern, and are unevenly distributed in the intrusion. Potassic alteration is distinct, and often contains veinlet/disseminated sulfide mineralization. Sericitization is most prevalent in the mining area, and is manifested as fine scaly aggregates in the metasomatic matrix. Mineralization intensity at Changdagou is clearly related to the alteration style. Strongly mineralized and highest grade (up to 1.64%) areas are mainly concentrated in the potassic and silicic zones. Low-grade mineralization (<0.4%) is also developed in/around the sericite zones.

### 3. Methods

#### 3.1. Zircon Morphology and Texture

Zircon separation was conducted on ~2 kg crushed rock sample at the Langfang Geological Laboratory (Langfang, China). Approximately 100–200 zircon grains from each sample were mounted in an epoxy resin disc. Before the U-Pb isotope analysis, all grains were observed under transmitted and reflected-light microscopy, as well as cathodoluminescence (CL) imaging to reveal their internal structure. All the CL imaging, U-Pb dating, trace element chemical and Hf isotopic analyses were performed at the Wuhan Sample Solution Analytical Technology Co. Ltd. (Wuhan, China). Zircon CL imaging was conducted with the Analytical Scanning Electron Microscope (JSMIT100, JEOL, Tokyo, Japan) connected to a GATAN MINICL system. The imaging conditions include 10,013.0 kV electric field and 8085  $\mu$ A current of tungsten filament.

#### 3.2. Zircon U-Pb Dating and Trace-Element Analyses

U-Pb dating and trace element analyses on zircon were simultaneously conducted with laser ablation-inductively coupled plasma-mass spectrometry (LA-ICP-MS). Detailed operating conditions for the laser ablation system and the ICP-MS instrument and data reduction are as described by Zong et al. [26]. The analyses were performed with a GeolasPro laser ablation system that consists of a COMPexPro 102 ArF excimer laser (193 nm wavelength and 200 mJ maximum energy) and a MicroLas optical system. An Agilent 7700e ICP-MS instrument (Agilent Technologies, Santa Clara, CA, USA) was used to acquire ion-signal intensities. Helium was used as a carrier gas, and argon was used as the make-up gas that mixed with the carrier gas via a T-connector before entering the ICP. A “wire” signal smoothing device is included in this laser ablation system [27]. The spot size and frequency of the laser were set to 32  $\mu$ m and 5 Hz, respectively. Zircon GJ-1 was used as the external standards for U-Pb dating and trace element calibration [28], respectively. Each analysis consists of a 20–30 s background acquisition followed by a 50 s sample data acquisition. In addition, the off-line selection and integration of background and analyzed signals, quantitative calibration for trace element analysis and time-drift correction and U-Pb dating were carried out with the Excel-based ICPMSDataCal software (Version 10.9, China University of Geosciences, Wuhan, China) [27]. The common lead correction was corrected with the measured  $^{204}\text{Pb}$  concentration [28,29]. Concordia diagrams and weighted mean calculations were calculated by the Isoplot/Ex\_ver3 [30].

#### 3.3. Zircon Hf Isotopic Analyses

The in-situ zircon Hf analyses were carried out by the Neptune multicollector (Thermo Fisher Scientific, Waltham, MA, USA) inductively coupled plasma-mass spectrometry (MC-ICP-MS) instrument equipped with a Geolas-193 laser ablation system at the Wuhan Sample Solution Analytical Technology Co. Ltd., Wuhan, China. During the analyses, a spot size of 44  $\mu$ m and laser repetition of 8 Hz with energy density of 5.3 J/cm<sup>2</sup> were used. Detailed operating conditions and procedures for the MC-ICP-MS analyses are as described in Hu et al. [27]. Notably, the spot locations of Hf isotopic analyses were presented in Figure 3. In addition, in-situ zircon Hf isotopes analysis requires

careful correction for isobaric interferences on  $^{176}\text{Hf}$  (e.g.,  $^{176}\text{Yb}$  and  $^{176}\text{Lu}$ ). It has been observed that the mass fractionation of Yb ( $\beta_{\text{Yb}}$ ) is not constant over time. Besides, the  $\beta_{\text{Yb}}$  obtained from the introduction of solutions is unsuitable for in situ zircon measurements [31]. The miscalculation of the  $\beta_{\text{Yb}}$  value will evidently affect the results of the  $^{176}\text{Hf}/^{177}\text{Hf}$  ratio. In this research, we used the directly obtained  $\beta_{\text{Yb}}$  value from the zircon grains in real-time. Moreover, the  $^{173}\text{Yb}/^{171}\text{Yb}$  and  $^{179}\text{Hf}/^{177}\text{Hf}$  values were applied to estimate the mass bias of Yb ( $\beta_{\text{Yb}}$ ) and Hf ( $\beta_{\text{Hf}}$ ), which were normalized to  $^{173}\text{Yb}/^{171}\text{Yb} = 1.13268$  and  $^{179}\text{Hf}/^{177}\text{Hf} = 0.73255$  [32] with an exponential correction for mass bias. Additionally, interference of  $^{176}\text{Yb}$  on  $^{176}\text{Hf}$  was corrected by measuring the interference-free  $^{173}\text{Yb}$  isotope and utilizing  $^{176}\text{Yb}/^{173}\text{Yb} = 0.79639$  [32] to calculate  $^{176}\text{Yb}/^{177}\text{Hf}$ . Similarly, the relatively minor interference of  $^{176}\text{Lu}$  on  $^{176}\text{Hf}$  was corrected by measuring the intensity of the interference-free  $^{175}\text{Lu}$  isotope and using the  $^{176}\text{Lu}/^{175}\text{Lu} = 0.02656$  [33] to estimate the  $^{176}\text{Lu}/^{177}\text{Hf}$  value. Because Yb and Lu have similar physicochemical properties, the  $\beta_{\text{Yb}}$  value was applied to calculate the mass fractionation of Lu. The off-line processing of analytical data (including mass bias calibrations, selection of samples, and blank signals) were performed by software ICPMSDataCal [27].



**Figure 3.** Cathodoluminescence (CL) images of zircons from the Changdagou granodiorite porphyry (sample CDG-01). The larger yellow circles represent locations of Hf isotopic analyses, whereas the smaller red circles indicate spots of LA-ICP-MS U-Pb dating. LA-ICP-MS = laser ablation-inductively coupled plasma-mass spectrometry.

### 3.4. Zircon Log $fO_2$ Estimation

Chemical compositions of zircon have been used to estimate the magma oxygen fugacity [34–37]. The rare earth element (REE) Ce has two valence states ( $Ce^{3+}$  and  $Ce^{4+}$ ) in magmas with different partition coefficients, and  $Ce^{4+}$  preferentially substitutes  $Zr^{4+}$  in zircon. Equation (1) was derived by ref. [34] to estimate the magma log  $fO_2$  on the basis of the relationship between Ce concentration and the Ti in zircon temperature (evaluated by the equation of Ferry and Watson [37]), estimated through high P-T experiments [38,39]. In addition, Loader et al. [40] argued that  $Ce_N/Ce_N^*$  (on the basis of the Nd-Sm method in zircon) is unlikely to be affected by mineral inclusions and is thus reliable. Hence, we calculated both  $Ce_N/Ce_N^*$  and log  $fO_2$  from the zircon compositions to unravel the magmatic redox state.  $Eu_N^*$  in this study is interpolated from the neighboring elements Sm and Gd, and is equal to  $(Sm_N \times Gd_N)^{1/2}$ .

$$\ln\left(\frac{Ce}{Ce^*}\right)_D = (0.1156 \pm 0.0050) \times \ln(fO_2) + \frac{13,860 \pm 708}{T(K)} - 6.125 \pm 0.484 \quad (1)$$

where  $(Ce/Ce^*)_D$  is the Ce anomaly in zircon grain, estimated from the partition coefficients, T is the absolute temperature of zircon crystallization.

### 3.5. Water Content Estimation

Currently, there are only a few methods for estimating magmatic  $H_2O$  content, including the use of plagioclase, hornblende, zircon hygrometer and melt inclusion analysis [38–44]. In addition, some whole-rock element parameters, like Sr/Y and  $\delta Eu$  values, can provide estimation of water content in PCD-forming magma [11,43,45]. Lu et al. [14] argued that zircon trace element ratios (e.g.,  $Eu_N/Eu_N^*$ ,  $Dy/Yb$ ,  $(Ce/Nd)/Y$ , and  $(Eu_N/Eu_N^*)/Y$ ) can serve as proxies for magmatic water content, and that PCD-fertile magmas commonly contain low  $Dy/Yb$  (<0.3) and high  $Eu_N/Eu_N^*$  (>0.3) ratios. It was interpreted that “wet” magmas can suppress early plagioclase crystallization, which causes the low  $Dy/Yb$  and high  $Eu_N/Eu_N^*$  ratios. However, the  $Eu_N/Eu_N^*$  ratios in zircon not only vary with water content but also with the redox state [14,34,45–47]. Hence, in this study,  $(Ce/Nd)/Y$  and  $Eu_N/Eu_N^*$  ratios are both selected as proxies for the water content of magma.

## 4. Results

### 4.1. Zircon U-Pb Age

For the zircon grains from Changdagou, CL imaging shows distinct concentric oscillatory zoning in most grains with no inherited cores. The U-Pb dating results are listed in Table 1 and illustrated in Figure 4. The Th/U ratios range from 0.32 to 1.14, distinctly higher than those of typical metamorphic zircons but resembling typical magmatic zircons [48,49]. The zircon grains yielded a weighted mean  $^{206}Pb/^{238}U$  age of  $214.97 \pm 0.98$  Ma (MSWD = 1.2,  $n = 30$ ). The U-Pb ages of cores and rims of the Changdagou zircon grains are identical [50].

**Table 1.** U-Pb isotopic compositions and ages of zircon grains from Changdagou granodiorite porphyry.

Samples	Element Composition (ppm)			Isotopic Element Ratio				Isotopic Ages (Ma)			
	Th	U	Th/U	<sup>207</sup> Pb/ <sup>235</sup> U		<sup>206</sup> Pb/ <sup>238</sup> U		<sup>207</sup> Pb/ <sup>235</sup> U		<sup>206</sup> Pb/ <sup>238</sup> U	
				Ratio	1σ	Ratio	1σ	Age	1σ	Age	1σ
CDG01-01	300	577	0.52	0.255596	0.008384	0.034111	0.000382	231.1	6.8	216.2	2.4
CDG01-02	547	739	0.74	0.230797	0.006918	0.033233	0.000315	210.9	5.7	210.8	2.0
CDG01-03	400	744	0.54	0.230956	0.007554	0.033618	0.000356	211.0	6.2	213.2	2.2
CDG01-04	300	930	0.32	0.231304	0.006904	0.033856	0.000468	211.3	5.7	214.6	2.9
CDG01-05	211	460	0.46	0.247813	0.009077	0.034124	0.000352	224.8	7.4	216.3	2.2
CDG01-06	385	629	0.61	0.234334	0.007178	0.034473	0.000414	213.8	5.9	218.5	2.6
CDG01-07	226	445	0.51	0.243863	0.008634	0.033403	0.000311	221.6	7.0	211.8	1.9
CDG01-08	492	684	0.72	0.245532	0.007382	0.033634	0.000344	222.9	6.0	213.3	2.1
CDG01-09	1222	1069	1.14	0.219964	0.006578	0.031091	0.000292	201.9	5.5	197.4	1.8
CDG01-10	256	508	0.50	0.238907	0.008682	0.033818	0.000345	217.5	7.1	214.4	2.2
CDG01-11	416	714	0.58	0.246925	0.007703	0.033763	0.000363	224.1	6.3	214.1	2.3
CDG01-12	176	428	0.41	0.250022	0.009253	0.034307	0.000432	226.6	7.5	217.4	2.7
CDG01-13	194	484	0.40	0.232775	0.009352	0.033610	0.000396	212.5	7.7	213.1	2.5
CDG01-14	483	766	0.63	0.254202	0.008857	0.034408	0.000438	230.0	7.2	218.1	2.7
CDG01-15	211	455	0.46	0.243216	0.008780	0.034336	0.000414	221.1	7.2	217.6	2.6
CDG01-16	131	349	0.38	0.239577	0.009104	0.033913	0.000403	218.1	7.5	215.0	2.5
CDG01-17	271	501	0.54	0.243990	0.009431	0.033704	0.000407	221.7	7.7	213.7	2.5
CDG01-18	107	280	0.38	0.250718	0.011693	0.033909	0.000412	227.2	9.5	215.0	2.6
CDG01-19	324	752	0.43	0.262268	0.008743	0.034951	0.000402	236.5	7.0	221.5	2.5
CDG01-20	240	522	0.46	0.220226	0.008393	0.034521	0.000392	202.1	7.0	218.8	2.4
CDG01-21	113	283	0.40	0.228462	0.009028	0.033838	0.000419	208.9	7.5	214.5	2.6
CDG01-22	229	470	0.49	0.238535	0.008811	0.033846	0.000376	217.2	7.2	214.6	2.3
CDG01-23	151	388	0.39	0.226945	0.007936	0.033975	0.000434	207.7	6.6	215.4	2.7
CDG01-24	229	470	0.49	0.221080	0.007490	0.033438	0.000349	202.8	6.2	212.0	2.2
CDG01-25	180	357	0.50	0.244226	0.008381	0.034059	0.000382	221.9	6.8	215.9	2.4
CDG01-26	253	442	0.57	0.234194	0.009242	0.033498	0.000375	213.7	7.6	212.4	2.3
CDG01-27	178	423	0.42	0.245466	0.009940	0.033892	0.000364	222.9	8.1	214.9	2.3
CDG01-28	281	576	0.49	0.241592	0.007813	0.034467	0.000325	219.7	6.4	218.4	2.0
CDG01-29	156	329	0.47	0.228488	0.009659	0.034469	0.000460	208.9	8.0	218.5	2.9
CDG01-30	192	465	0.41	0.236486	0.007728	0.033521	0.000318	215.5	6.3	212.5	2.0
GJ-1	9.43	307	0.03	0.7644	0.0255	0.0984	0.0011	577	14.65	605	6.59
GJ-1	9.37	308	0.03	0.7994	0.0251	0.0969	0.0011	596	14.19	596	6.30
GJ-1	9.64	297	0.03	0.8183	0.0213	0.0978	0.0010	607	11.91	602	5.97
GJ-1	9.86	298	0.03	0.8009	0.0223	0.0968	0.0010	597	12.59	596	5.75
GJ-1	9.41	297	0.03	0.7797	0.0234	0.0976	0.0011	585	13.35	600	6.75
GJ-1	9.57	302	0.03	0.7983	0.0241	0.0968	0.0011	596	13.59	596	6.32
GJ-1	9.66	298	0.03	0.8322	0.0217	0.0978	0.0010	615	12.02	601	5.95
GJ-1	9.58	299	0.03	0.7979	0.0240	0.0985	0.0010	596	13.58	606	5.66

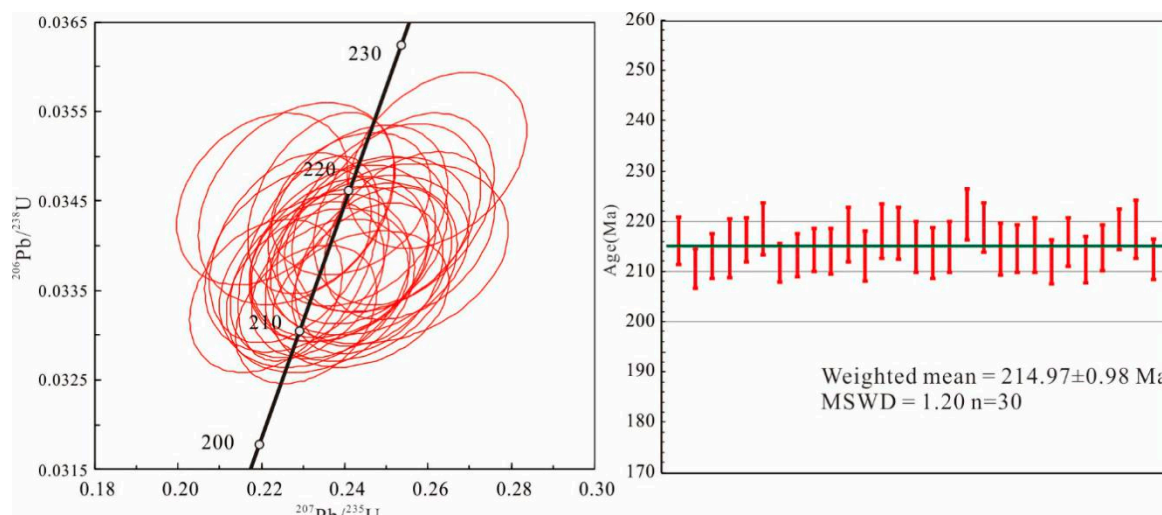


**Figure 4.** Zircon U-Pb Concordia and  $^{206}\text{Pb}/^{238}\text{Pb}$  weighted mean age diagrams for the Changdagou granodiorite porphyry.

#### 4.2. Zircon Trace Element Compositions

Zircon trace elements data of the Changdagou granodiorite are presented in Table 2, and the chondrite-normalized REE (Rare Earth element) patterns are shown in Figure 5. All the zircon grains are LREE (Light Rare Earth Element)-depleted and HREE (Heavy Rare Earth Element)-enriched. Concentrations of Ce and Eu are of 3.4–106 ppm and 0.14–0.75 ppm, respectively. All zircon samples show strong positive Ce anomalies ( $\text{Ce}_N/\text{Ce}_N^* = 14$  to 172) and slightly negative Eu anomalies ( $\text{Eu}_N^* = 0.09$  to 0.32). These characters resemble those of typical magmatic zircon [48].

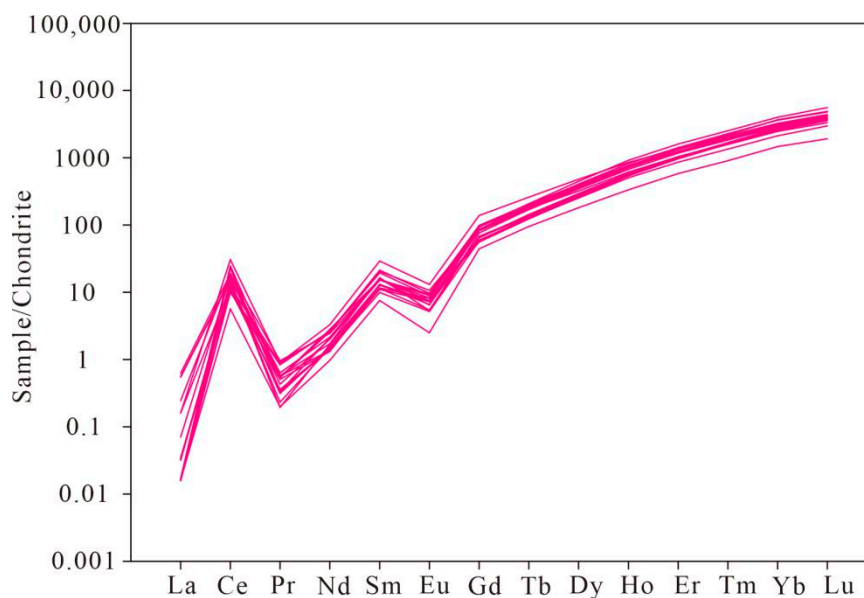


**Figure 5.** Chondrite-normalized REE diagram of zircon grains from the Changdagou granodiorite porphyry. Normalizing values from [48,49].

**Table 2.** Trace element concentrations of zircon grains from Changdagou granodiorite porphyry.

Samples	Ti	Y	La	Ce	Pr	Nd	Sm	Eu	Gd	Tb	Dy	Ho	Er	Tm	Yb	P	Hf
CDG01-01	7.05	1324	0.132	9.89	0.06	1	2.41	0.38	17.58	6.93	99	44	221	54	555	382	10,978
CDG01-02	5.11	1211	10.41	33.41	2.78	11.86	4.07	0.74	19.02	6.74	90	38	195	47	493	605	11,436
CDG01-03	2.79	1587	0.004	15.15	0.05	1.21	2.98	0.51	19.26	7.74	113	52	265	64	681	398	12,002
CDG01-04	2.9	1256	b.d.	5.45	0.02	1.16	2.04	0.17	15.01	6.3	88	41	216	56	615	340	12,736
CDG01-05	4.21	1001	0.008	8.46	0.02	0.7	1.99	0.38	13.55	4.99	71	32	168	42	461	365	11,900
CDG01-06	3.64	1074	8.014	29.05	2.25	10.97	3.41	0.54	16.97	5.85	78	35	175	42	463	539	12,201
CDG01-07	2.23	1022	0.008	8.51	0.03	0.72	1.74	0.32	13.94	5.13	71	33	168	41	435	350	11,657
CDG01-08	2.84	1258	0.017	10.34	0.04	0.94	2.35	0.48	19.51	7.05	95	41	204	47	478	410	11,449
CDG01-09	4.16	1465	0.038	18.82	0.09	1.53	4.43	0.76	28.34	9.73	122	48	225	51	512	342	12,681
CDG01-10	2.05	873	0.008	6.67	0.03	0.66	1.52	0.3	11.96	4.69	64	29	143	34	359	589	12,359
CDG01-11	4.78	1092	44.713	106.16	12.5	55.33	12.01	0.51	24.76	7.2	88	36	175	41	416	341	11,535
CDG01-12	3.8	982	0.008	7.25	0.05	0.62	1.77	0.47	11.5	4.6	66	30	160	41	444	365	11,951
CDG01-13	3.98	1174	b.d.	7.7	0.02	0.83	1.96	0.3	13.97	5.73	83	37	194	48	508	390	12,297
CDG01-14	2.58	1292	0.004	14.02	0.03	0.98	2.33	0.52	17.23	6.77	95	41	208	51	538	363	11,644
CDG01-15	5597	1052	0.13	9.57	0.05	0.64	1.95	0.43	13.32	5.35	75	33	172	42	458	322	12,351
CDG01-16	3.68	721	b.d.	5.53	0.02	0.34	1.47	0.3	8.68	3.37	49	23	119	31	343	428	11,130
CDG01-17	4.03	1277	0.038	7.4	0.08	1.2	3.28	0.56	20.26	7.66	101	42	203	49	509	348	11,229
CDG01-18	3.18	750	b.d.	3.95	0.04	0.49	1.56	0.34	10.2	4.03	54	24	125	31	335	381	12,121
CDG01-19	4.1	1319	0.149	11.49	0.09	1.14	2.35	0.54	17.54	6.45	94	41	221	56	624	397	11,235
CDG01-20	3.69	1476	b.d.	10.69	0.04	1.03	2.8	0.56	17.95	7.39	105	47	244	59	612	297	11,601
CDG01-21	2.74	593	0.004	3.48	0.02	0.46	1.16	0.14	9.07	3.55	46	19	96	23	249	622	11,447
CDG01-22	2.97	1206	1.921	13.54	0.63	3.35	3.1	0.52	16.54	5.87	83	38	194	48	520	304	12,036
CDG01-23	2.23	794	b.d.	5.98	0.03	0.61	1.35	0.25	10.64	4.02	54	25	129	33	358	378	11,304
CDG01-24	1.52	1272	0.004	9.26	0.02	0.78	2.01	0.42	16.87	6.37	89	40	206	50	523	338	11,157
CDG01-25	2.36	1081	0.004	6.08	0.08	1.23	3.12	0.62	17.13	6.6	81	35	172	40	418	415	10,100
CDG01-26	4.95	1635	b.d.	9.11	0.05	1.18	2.46	0.58	19.9	8.29	120	54	263	62	643	335	11,568
CDG01-27	3.43	1014	0.008	8.15	0.03	0.67	1.69	0.42	12.22	4.86	68	32	167	43	468	387	11,428
CDG01-28	2.91	1444	0.058	11.59	0.05	1.3	2.38	0.44	17.82	7.31	103	47	234	58	614	305	11,514
CDG01-29	1.93	687	b.d.	4.78	0.03	0.48	1.25	0.2	8.83	3.6	49	22	113	27	297	349	11,722
CDG01-30	3.62	1184	0.004	6.47	0.05	0.8	2.52	0.31	15.59	6.39	87	38	194	47	492	437	11,958

Note: "b.d." represent the concentration below the detection limit.

The calculated  $\log fO_2$  values are listed in Table A1 and plotted in Figure 6a. In the  $\log fO_2$ – $T$  diagram, the Changdagou granodiorite porphyry data plot between the FMQ and MH buffers. For the data from the Pulang and Lannitang PCDs (southern Yidun arc), the Lannitang porphyry samples mainly plot above the NNO buffer, whilst half of the Pulang samples plot above the MH buffer. Therefore, the Pulang (FMQ  $-9.25$  to  $+13.22$ ) and Lannitang (FMQ  $+0.23$  to  $+9.52$ ) granites have higher  $\log fO_2$  than the Changdagou granites (FMQ  $-3.14$  to  $+7.44$ ) (Figure 6b). Zircon grains of Changdagou granodiorite have relatively low Ti contents (1.51–7.04 ppm), which gave Ti-in-zircon temperatures of 628 to 757 °C (avg. 689 °C). In the  $\log fO_2$ – $T$  diagram, the Changdagou granodiorite has a lower Ti-in-zircon temperature than those of the Pulang and Lannitang granites.

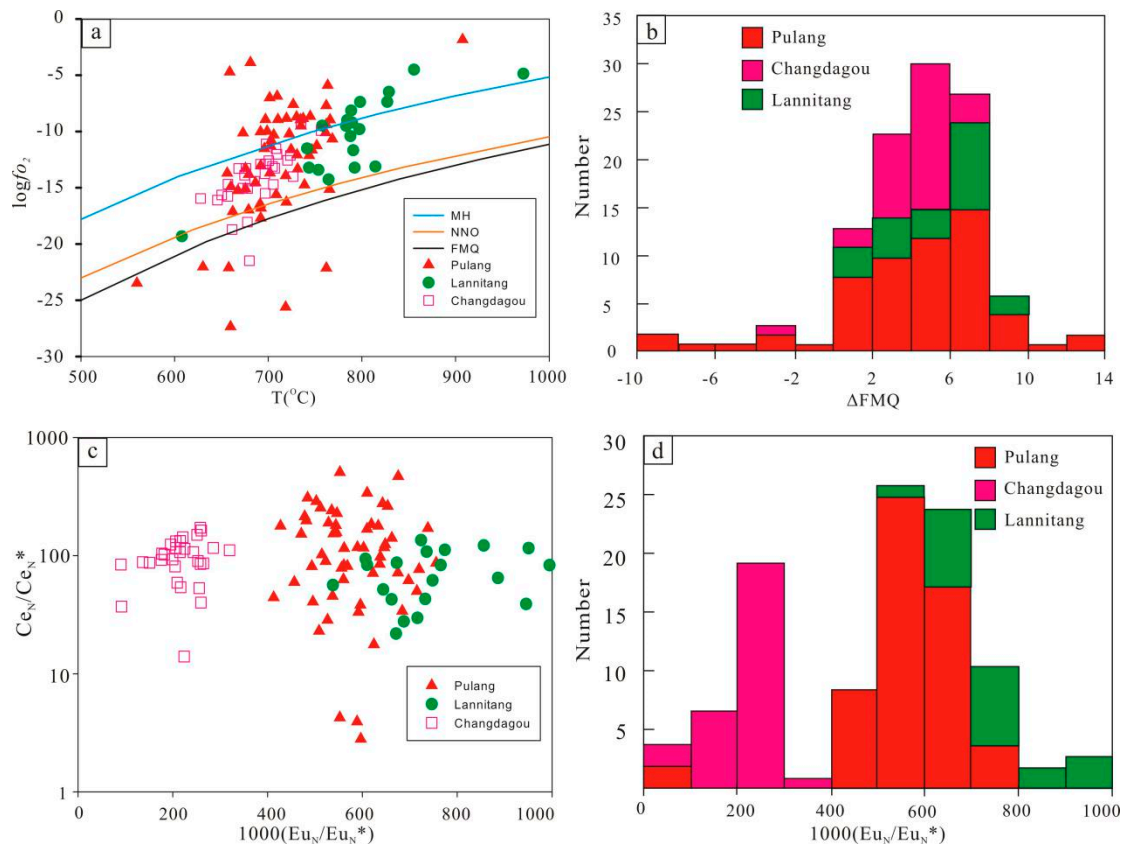


**Figure 6.**  $Ce_N/Ce_N^*$ -related binary diagrams of zircon grains for the Changdagou, Pulang and Lannitang granites from Yidun arc. (a)  $\log fO_2$  vs. temp. °C diagram, where  $\log fO_2$  value was calculated by the method of Trail et al. [34]; (b) Histogram of oxygen fugacity; (c)  $Ce_N/Ce_N^*$  vs.  $Eu_N/Eu_N^*$  plot, where  $Ce_N^*$  is calculated by fitting method; (d) Histogram of  $1000(Eu_N/Eu_N^*)$  vs. Data are as listed in Table A1.

As shown in Figure 6c,d, Changdagou granite shows a lower and narrower range of zircon  $Eu_N/Eu_N^*$  values (0.1–0.32; avg. 0.22) than those of the Lannitang (0.54–0.99; avg. 0.75) and Pulang (0.41–0.76; avg. 0.56) granites. Zircon  $Ce_N/Ce_N^*$  values of the Changdagou sample (14–172; avg. 98) have a similar range with their Lannitang (22–135; avg. 73) and Pulang (3–507; avg. 143) counterparts (Table A1). Besides, it was found that the  $Ce_N/Ce_N^*$  and  $Eu_N/Eu_N^*$  does not have any positive relationship.

The zircon  $Eu_N/Eu_N^*$  vs.  $(Ce/Nd)/Y$  diagram shows marked distinction between the Changdagou and Pulang granites (Lannitang granites not shown due to the lack of published zircon Y data). The Changdagou granites show lower zircon  $(Ce/Nd)/Y$  ratios (0.002–0.022; avg. 0.009) than their Pulang counterparts (0.007–0.18; avg. 0.038), and there is a positive correlation between  $Eu_N/Eu_N^*$  and  $(Ce/Nd)/Y$  ratios (Figure 7).

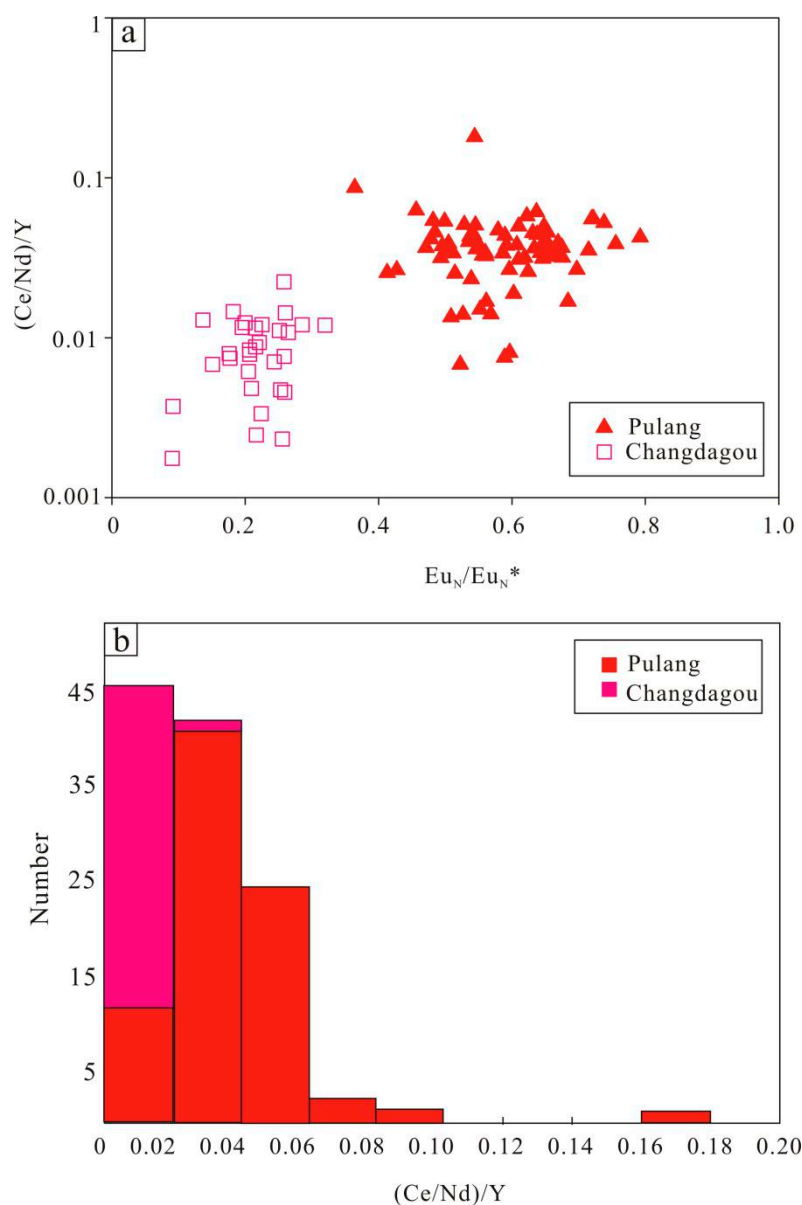


**Figure 7.** (a) (Ce/Nd)/Y vs.  $Eu_N/Eu_N^*$  diagram of zircon grains for the Changdagou and Pulang porphyries; (b) histogram of (Ce/Nd)/Y values.

#### 4.3. Zircon Hf Isotopes

Hf-isotopic data of the zircon grains analyzed from the Changdagou granodiorite porphyry (CDG01) are shown in Table 3. Zircon GJ-1 and 91,500 was used as the reference standard, with weighted mean  $^{176}\text{Hf}/^{177}\text{Hf}$  ratios of  $0.282017 \pm 0.0000060$  and  $0.282308 \pm 0.0000035$ , respectively, determined by our routine analyses. The zircon  $\epsilon\text{Hf}(t)$  values vary in a narrow range (−2.9 to −4.9; avg. −3.4), corresponding to the lower crust (Figure 8a). Comparatively, the Pulang granites have higher zircon  $\epsilon\text{Hf}(t)$  values (−4.7 to 2.5; [6]), which plot above the Chondrite Uniform Reservoir (CHUR) evolutionary line in the  $\epsilon\text{Hf}(t)$  vs. U-Pb age diagram (Figure 8).

**Table 3.** Hf isotopes in zircon grains from Changdagou granodiorite porphyry.

Samples	$^{176}\text{Hf}/^{177}\text{Hf}$	1 $\sigma$	$^{176}\text{Lu}/^{177}\text{Hf}$	1 $\sigma$	$^{176}\text{Yb}/^{177}\text{Hf}$	1 $\sigma$	$\epsilon\text{Hf}(0)$	$\epsilon\text{Hf}(t)$	TDM(Ma)	TDMC(Ma)
CDG01-01	0.282549	0.000008453	0.001543	0.00002525	0.041931	0.000585	−8.33	−3.78	1009	1466
CDG01-02	0.282553	0.000007740	0.001566	0.00001218	0.041916	0.000406	−8.22	−3.66	1005	1458
CDG01-03	0.282568	0.000007793	0.001337	0.00001767	0.036474	0.000564	−7.66	−3.08	976	1421
CDG01-05	0.282573	0.000008512	0.001580	0.00000861	0.042021	0.000185	−7.48	−2.93	975	1412
CDG01-06	0.282556	0.000008577	0.001426	0.00000996	0.039120	0.000397	−8.09	−3.51	996	1449
CDG01-07	0.282569	0.000008165	0.001459	0.00000939	0.039605	0.000191	−7.63	−3.06	978	1420
CDG01-08	0.282556	0.000007987	0.001472	0.00001568	0.039988	0.000302	−8.09	−3.52	997	1450
CDG01-11	0.282520	0.000008477	0.001970	0.00004212	0.057167	0.001163	−9.37	−4.88	1063	1536
CDG01-12	0.282565	0.000007780	0.001549	0.00003119	0.042051	0.000783	−7.77	−3.21	986	1430
CDG01-13	0.282561	0.000009007	0.001495	0.00001240	0.039560	0.000151	−7.93	−3.36	991	1439
CDG01-15	0.282574	0.000008591	0.001298	0.00001065	0.035959	0.000402	−7.47	−2.87	967	1408
CDG01-16	0.282575	0.000007749	0.000731	0.00001281	0.019467	0.000398	−7.41	−2.74	951	1400
CDG01-19	0.282561	0.000008847	0.001569	0.00001555	0.043378	0.000470	−7.93	−3.37	993	1440
CDG01-20	0.282560	0.000008137	0.001528	0.00002673	0.042351	0.000834	−7.94	−3.39	993	1441
CDG01-21	0.282570	0.000007521	0.000859	0.00000944	0.023062	0.000150	−7.62	−2.96	962	1414
CDG01-22	0.282546	0.000007604	0.001355	0.00000275	0.037267	0.000181	−8.44	−3.86	1008	1471
CDG01-25	0.282560	0.000007855	0.001161	0.00000818	0.031958	0.000242	−7.97	−3.36	984	1439
CDG01-26	0.282538	0.000009456	0.002075	0.00003579	0.057039	0.000774	−8.73	−4.24	1039	1496
CDG01-27	0.282549	0.000008600	0.001454	0.00002130	0.039899	0.000614	−8.33	−3.76	1006	1465
CDG01-30	0.282565	0.000007378	0.001037	0.00001720	0.028808	0.000593	−7.78	−3.15	973	1426

Note:  $\epsilon\text{Hf}(t) = 10,000 \times \{[(^{176}\text{Hf}/^{177}\text{Hf})_S - (^{176}\text{Lu}/^{177}\text{Hf})_S \times (e^{\lambda t} - 1)] / [(^{176}\text{Hf}/^{177}\text{Hf})_{\text{CHUR},0} - (^{176}\text{Lu}/^{177}\text{Hf})_{\text{CHUR}} \times (e^{\lambda t} - 1)] - 1\}$ .  $\text{TDM}_1 = 1/\lambda \times \ln\{1 + [(^{176}\text{Hf}/^{177}\text{Hf})_S - (^{176}\text{Hf}/^{177}\text{Hf})_{\text{DM}}] / [(^{176}\text{Lu}/^{177}\text{Hf})_S - (^{176}\text{Lu}/^{177}\text{Hf})_{\text{DM}}]\}$ .  $\text{TDM}_2 = t_{\text{DM}} - (t_{\text{DM}} - t) \times [(f_{\text{cc}} - f_s) / (f_{\text{cc}} - f_{\text{DM}})]$ .  $(^{176}\text{Lu}/^{177}\text{Hf})_{\text{CHUR}} = 0.0332$ ,  $(^{176}\text{Hf}/^{177}\text{Hf})_{\text{CHUR},0} = 0.282772$ ,  $(^{176}\text{Lu}/^{177}\text{Hf})_{\text{DM}} = 0.0384$  and  $(^{176}\text{Hf}/^{177}\text{Hf})_{\text{DM}} = 0.28325$ ;  $(^{176}\text{Lu}/^{177}\text{Hf})_{\text{mean crust}} = 0.015$ .  $f_{\text{cc}} = [(^{176}\text{Lu}/^{177}\text{Hf})_{\text{mean crust}} / (^{176}\text{Lu}/^{177}\text{Hf})_{\text{CHUR}}] - 1$ ;  $f_s = f_{\text{Lu}/\text{Hf}}$ ;  $f_{\text{DM}} = [(^{176}\text{Lu}/^{177}\text{Hf})_{\text{DM}} / (^{176}\text{Lu}/^{177}\text{Hf})_{\text{CHUR}}] - 1$ ;  $t$  = crystallization time of zircon [51,52].

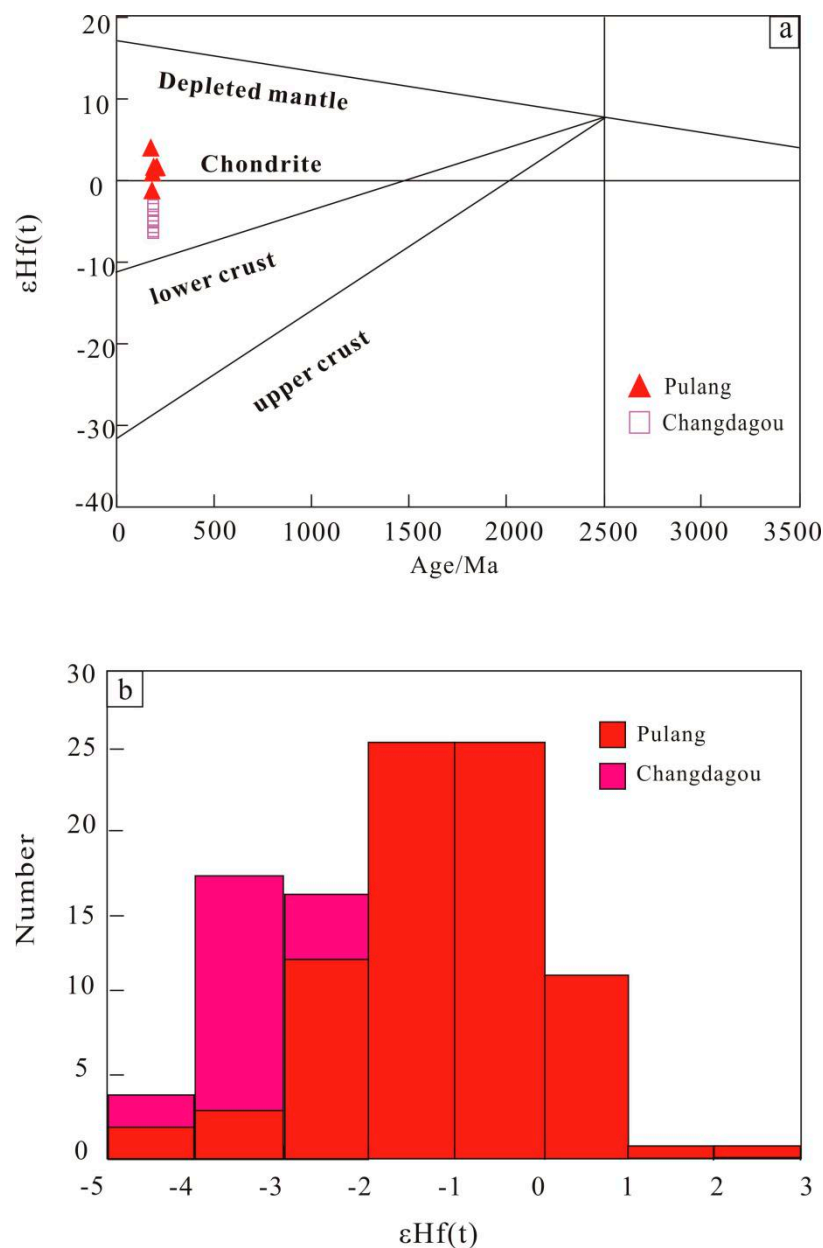


Figure 8. (a) Diagram of  $\epsilon\text{Hf}(t)$  vs. U-Pb ages. (b) Histogram of  $\epsilon\text{Hf}(t)$  values.

## 5. Discussion

### 5.1. Geochronological Data

The age of Changdagou granite has long been estimated by its intrusive relationship with the regional stratigraphy [53]. In this study, we report the first zircon U-Pb age for the ore-forming Changdagou granodiorite porphyry ( $214.97 \pm 0.98$  Ma) from the northern Yidun arc. In the southern Yidun arc, Wang et al. [6] reported three zircon U-Pb ages ( $214.3 \pm 2.9$  Ma,  $211.6 \pm 3.1$  Ma, and  $214.1 \pm 2.9$  Ma) for the Pulang complex, Chen et al. [54] reported one zircon U-Pb age ( $216.7 \pm 1.2$  Ma) for the Lannitang porphyry, and Ren et al. [55] reported one zircon U-Pb age ( $213.4 \pm 1.5$  Ma) for the Xuejiping porphyry. All these ages, no matter whether from the northern or southern segment of the Yidun arc, fall consistently into the Late Triassic, coeval with the Indosinian Orogeny in SW China and mainland SE Asia. With the lithological and geochemical features of the igneous–sedimentary assemblages in the region, it is broadly accepted that the Yidun zone was a continental arc developed

on the Zhongza Block [2,4]. Thus, formation of the Changdagou granodiorite porphyry was probably related to the subduction associated with Late Triassic magmatism in the Yidun zone [23,56,57].

### 5.2. Magma Redox State

It is generally accepted that oxidized magmas are favorable to the formation of PCDs, via inhibiting early sulfide precipitation and allowing the ore metals to be concentrated into the residual melt and hydrothermal fluids [11,58–60]. Shen et al. [58] argued that the oxygen fugacity has a positive relationship with the size of PCDs in the CAOB, and that the  $(\text{NNO} + 2)$  values can distinguish large and intermediate PCDs from small ones. In this study, the average magmatic oxygen fugacity (FMQ +3.98) and  $\text{Ce}_\text{N}/\text{Ce}_\text{N}^*$  (98) for the Changdagou granodiorite are much higher than the lowest limit (FMQ + 1.5) for porphyry Cu–(Au)–Mo mineralization [61–63]. These data suggest that Changdagou granodiorite has PCD-forming potential. Meanwhile, the Pulang and Lannitang granites both contain higher  $\log f\text{O}_2$  values than those of the Changdagou granodiorite (Figure 6a,b), which may explain why the PCDs at Pulang (1.14 Mt) and Lannitang (0.30 Mt for Xuejiping) are larger than that at Changdagou [7].

### 5.3. Magma Water Content

High magmatic water contents are widely accepted to be important in enhancing the magma PCD fertility [38,39,41,59–63]. Lu et al. [14] suggested that the fertile magmas commonly contain high  $(\text{Ce}/\text{Nd})/\text{Y}$  and high  $\text{Eu}_\text{N}/\text{Eu}_\text{N}^*$  ratios. However,  $\text{Eu}_\text{N}/\text{Eu}_\text{N}^*$  of zircon grain is also dependent on the magma oxidation state [5,31,40,46]. In this study, the lack of positive  $\text{Ce}_\text{N}/\text{Ce}_\text{N}^*$  vs.  $\text{Eu}_\text{N}/\text{Eu}_\text{N}^*$  correlation, and the presence of positive  $\text{Eu}_\text{N}/\text{Eu}_\text{N}^*$  vs.  $(\text{Ce}/\text{Nd})/\text{Y}$  correlation suggest that  $\text{Eu}_\text{N}/\text{Eu}_\text{N}^*$  is probably affected by water content (Figures 6c and 7a). The Changdagou granodiorite porphyry has a narrower and lower  $\text{Eu}_\text{N}/\text{Eu}_\text{N}^*$  zircon grain range than those of the Lannitang and Pulang granites, which suggest that the latter two have higher magmatic water contents.

### 5.4. Tectono-Metallogenic Implications on the Northern and Southern Yidun Arc

It has been generally believed that high oxidization of arc magmas are related to subduction: the closer the distance of the arc magmas from the subduction zone, the higher the oxygen fugacity [10,12,37,43,64–66]. This is likely caused by the larger amount of oxidized ions (i.e.,  $\text{Fe}^{3+}$ ,  $\text{Mn}^{4+}$ ,  $\text{S}^{6+}$ , and  $\text{C}^{4+}$ ) carried by the slab-derived fluids closer to the subduction front [10,67–70]. In this study, we suggest that ore-forming magmas at Lannitang and Pulang (southern Yidun arc) have had higher water content and oxygen fugacity than those at Changdaou (northern Yidun arc), which implies that the southern Yidun arc was closer to the Ganzi-Litang subduction zone. A similar conclusion was also reached by Wang et al. [6].

In contrast with Lu, Hf partitions into silicate melts more efficiently, melts derived from the magma would become less radiogenic (lower  $^{176}\text{Lu}/^{176}\text{Hf}$ ) and thus have lower  $^{176}\text{Hf}/^{177}\text{Hf}$  ratios relative to the residue [54,71]. Regional intrusions sourced from the continental crust generally possess low  $\epsilon\text{Hf}(t)$  values, such as Hongshan quartz monzonite [6]. The Changdagou sample plot is close to the chondrite line and presents variations in  $\epsilon\text{Hf}(t)$  values (Figure 8a,b). It is arranged with the coeval Late Triassic intrusions in the Songpan-Ganzi terrane [72].

As shown in Figure 9, most of the Late Triassic intrusions in the southern Yidun arc, including the Xuejiping, Pulang, Lannitang, and Songnuo intrusions, are PCD-forming, but coeval granites in the northern Yidun arc are mostly ore-barren, such as the Daocheng and Cuojiama intrusions [3]. These infertile rocks show a wide range of negative  $\epsilon\text{Hf}(t)$  values, indicating a mixed source dominated by crustal components [73,74]. Unlike most other Late Triassic intrusions in the northern Yidun arc, the  $\epsilon\text{Hf}(t)$  values of Changdagou granodiorite porphyry presents a narrow range which cluster around 0, indicating a more mantle-derived source. The decreasing  $\epsilon\text{Hf}(t)$  trend from south to north (and reverses sharply around Changdagou) in the Yidun arc probably indicate decreasing mantle-derived input to the granitoid formation from south to north, which may be attributed to the shape of the continental arc and/or subduction angle variation [3,4,6].

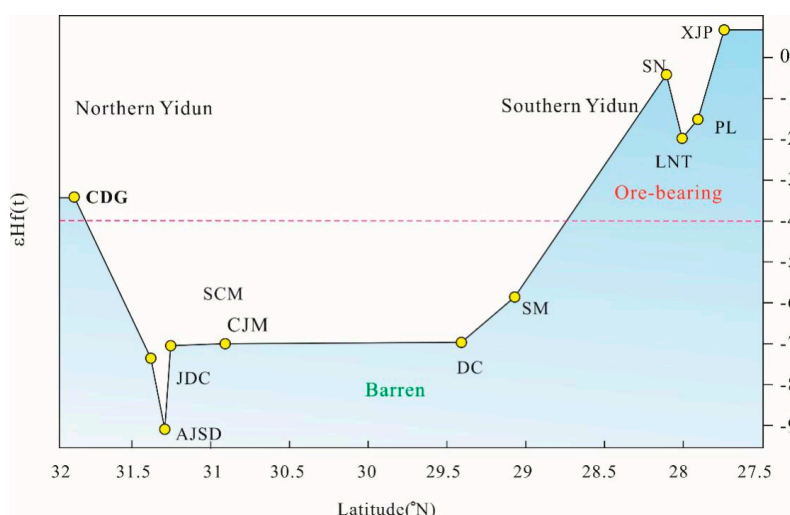


**Figure 9.** Diagram of  $\epsilon_{\text{Hf}}(t)$  vs. latitude to illustrate the contribution of mantle components for the ore-fertile granites from north to south in the Yidun arc. The data are from refs. [4,6]. Abbreviations: CDG—Changdagou; SCM—Sucuoma; AJSD—Ajisenduo; JDC—Jiaduocuo; CJM—Cuojiama; LNT—Lannitang; PL—Pulang; SM—Shenmu; SN—Songnuo; XJP—Xuejiping; DC—Daocheng.

## 6. Conclusions

1. Zircon U-Pb dating of the Changdagou granodiorite porphyry in the northern Yidun arc yielded  $214.97 \pm 0.98$  Ma. This age is very similar to other Late Triassic PCD-forming magmatisms in the Yidun arc.

2. As reflected by proxies such as  $\log f_{\text{O}_2}$ ,  $\text{Eu}_{\text{N}}/\text{Eu}_{\text{N}}^*$ , and  $(\text{Ce}/\text{Nd})/\text{Y}$ , magmas that formed the Changdagou granodiorite porphyry may have had high oxygen fugacity ( $\text{FMQ} + 3.98$ ) and water content, yet they were likely lower than those of the Pulang and Langnitang ore-causative porphyries. This may have limited the PCD size at Changdagou.

3. The southern segment of the Yidun arc was probably closer to the subduction front than the northern segment, where Changdagou is located. The more subduction-distal setting of the northern Yidun arc may have resulted in the lower oxygen fugacity, water content, enriched-mantle input, and thus the PCD-fertility there.

**Author Contributions:** X.-Y.L. and H.S. conceived and designed the experiments; X.-Y.L. performed the experiments; J.-R.Z. and X.-Y.L. analyzed the data; X.-Y.L. wrote the paper, assisted by all other authors; and C.-K.L. revised the paper.

**Funding:** This research was funded by the NSFC-China (418030401 and 41802251), the Geological Survey of China (1212011220391), and the China Scholarship Council Fund (201406380063).

**Acknowledgments:** We are grateful to Wei Gao for helping with the LA-ICP-MS analyses. Also, we appreciate the constructive comments and suggestions by the editor and three anonymous reviewers, with which the paper was greatly improved.

**Conflicts of Interest:** The authors declare no conflict of interest.

## Appendix A

**Table A1.** Crystallization temperatures, Eu and Ce anomalies, and magma oxygen fugacity of zircon grains from Changdagou, Pulang, and Lannitang granites.

Spot. No	T (Ti in Zircon)	CeN/CeN*	logfO <sub>2</sub>	δFMQ	EuN/EuN*	Ce/Nd/Y
<b>Changdagou Granite</b>						
CDG01-01	757	104	−9.92	6.29	0.18	0.00744
CDG01-02	727	53	−14.01	3	0.26	0.00233
CDG01-03	675	116	−13.88	4.62	0.21	0.00788
CDG01-04	678	37	−18.06	0.35	0.09	0.00373
CDG01-05	709	114	−12.03	5.46	0.23	0.01207
CDG01-06	697	54	−15.5	2.34	0.22	0.00247
CDG01-07	657	124	−14.68	4.37	0.2	0.01158
CDG01-08	676	133	−13.28	5.17	0.22	0.00877
CDG01-09	708	132	−11.53	5.98	0.21	0.00838
CDG01-10	650	107	−15.64	3.62	0.22	0.01149
CDG01-11	721	84	−12.56	4.61	0.09	0.00176
CDG01-12	701	111	−12.6	5.14	0.32	0.01198
CDG01-13	705	92	−13.1	4.52	0.18	0.00795
CDG01-14	668	150	−13.29	5.41	0.25	0.01111
CDG01-15	735	163	−9.34	7.44	0.26	0.01429
CDG01-16	698	172	−11.1	6.72	0.26	0.02233
CDG01-17	705	59	−14.72	2.88	0.21	0.00482
CDG01-18	685	86	−14.42	3.76	0.26	0.01078
CDG01-19	707	85	−13.27	4.29	0.26	0.00766
CDG01-20	698	107	−12.88	4.93	0.24	0.00706
CDG01-21	673	88	−15.04	3.51	0.14	0.01289
CDG01-22	680	14	−21.48	−3.14	0.22	0.00335
CDG01-23	657	93	−15.77	3.28	0.2	0.01239
CDG01-24	628	143	−15.95	4.05	0.22	0.00933
CDG01-25	661	40	−18.72	0.19	0.26	0.00456
CDG01-26	724	90	−12.13	4.96	0.25	0.00472
CDG01-27	692	116	−12.91	5.08	0.29	0.01205
CDG01-28	678	81	−15.07	3.33	0.2	0.00615
CDG01-29	646	102	−16.1	3.31	0.18	0.01455
CDG01-30	696	87	−13.75	4.1	0.15	0.00681
<b>Pulang Complex</b>						
PL1	710	469	−6.86	9.72	0.68	0.031762
PL2	907	168	−1.83	10.58	0.61	0.030845
PL3	762	117	−9.39	5.94	0.65	0.031273
PL4	712	-			0.58	0.04695
PL5	739	38	−14.75	1.12	0.6	0.026624
PL6	598	-			0.65	0.036933
PL7	658	18	−22.12	−4.15	0.62	0.02585
PL8	701	507	−7.01	9.78	0.55	0.036627
PL9	768	77	−10.67	4.51	0.72	0.055079
PL10	687	-			0.79	0.042448
PL11	744	72	−12.14	3.61	0.67	0.036617
PL012	656	170	−13.71	4.31	0.74	0.052305
PL013	701	-			0.72	0.055537
PL14	676	87	−15.09	2.38	0.76	0.038616
PL15	681	1586	−3.87	13.46	0.61	0.03808

Table A1. Cont.

Spot. No	T (Ti in Zircon)	CeN/CeN*	logfO <sub>2</sub>	δFMQ	EuN/EuN*	Ce/Nd/Y
<b>Pulang Complex</b>						
PL16	692	262	−10.02	7.02	0.65	0.045514
PL17	719	63	−13.92	2.43	0.56	0.033955
PL18	735	189	−8.95	7.02	0.53	0.050858
PL19	745	178	−8.66	7.06	0.63	0.036346
PL20	560	71	−23.48	−2.43	0.62	0.057586
PL21	692	34	−17.69	−0.65	0.68	0.016862
PL22	679	50	−16.97	0.41	0.72	0.035223
PL23	679	115	−13.81	3.56	0.56	0.01685
PL024	703	181	−10.79	5.96	0.54	0.180001
PL021	761	98	−10.1	5.24	0.64	0.04412
PL022	685	-			0.59	0.033711
PL023	762	4	−22.14	−6.81	0.59	0.007535
PL024	719	241	−8.84	7.5	0.54	0.039809
PL025	752	81	−11.26	4.3	0.57	0.014062
PL026	692	118	−13.03	4.01	0.59	0.043575
PL027	719	33	−16.28	0.06	0.59	0.037696
PL028	762	184	−7.7	7.63	0.62	0.031683
PL029	747	79	−11.64	4.03	0.56	0.032735
PL-S210	630	28	−22.03	−3.27	0.53	0.013966
PL-S11	660	116	−14.91	3	0.6	0.018867
PL-S12	730	214	−8.71	7.36	0.48	0.041371
PL-S13	673	339	−10.13	7.42	0.61	0.04972
PL-S14	666	-			0.65	0.041221
PL-S15	766	125	−8.96	6.27	0.65	0.049746
PL-S16	686	85	−14.56	2.62	0.64	0.061066
PL-S17	753	-			0.36	0.08668
PL-S18	706	198	−10.31	6.37	0.48	0.053921
PL-S19	659	1792	−4.71	13.23	0.63	0.045295
PL-S20	660	4	−27.36	−9.45	0.55	0.015036
PL-S21	680	-			0.67	0.039204
PL-S22	719	3	−25.61	−9.25	0.6	0.008073
PL-S23	676	141	−13.28	4.19	0.66	0.03328
PL-S24	731	62	−13.33	2.71	0.7	0.026698
PL031	731	-			0.66	0.032214
PL032	696	157	−11.52	5.41	0.55	0.050453
PL033	724	102	−11.61	4.6	0.51	0.025244
PL034	737	-			0.5	0.03888
PL035	692	41	−16.81	0.22	0.5	0.037543
PL036	727	288	−7.6	8.56	0.5	0.034121
PL037	764	277	−5.9	9.39	0.64	0.03397
PL038	737	178	−8.85	7.05	0.43	0.026517
PL039	739	-			0.5	0.053342
PL0310	735	154	−9.52	6.44	0.54	0.04403
PL0311	702	81	−13.69	3.09	0.49	0.031541
PL0312	697	308	−8.93	7.97	0.48	0.045628
PL0313	662	60	−17.11	0.73	0.46	0.062515
PL0314	668	90	−15.26	2.44	0.52	0.006801
PL0315	722	152	−10.21	6.05	0.47	0.036551
PL0316	699	228	−9.98	6.89	0.55	0.035842
PL0317	765	23	−15.15	0.1	0.51	0.01347
PL0318	709	44	−15.61	1	0.41	0.025461
PL0319	710	254	−8.94	7.63	0.51	0.033803
PL0320	702	153	−11.27	5.5	0.54	0.023279
PL0321	691	45	−16.45	0.61	0.54	0.042942
PL0322	731	83	−12.08	3.98	0.56	0.032442

Table A1. Cont.

Spot. No	T (Ti in Zircon)	CeN/CeN*	logfO <sub>2</sub>	δFMQ	EuN/EuN*	Ce/Nd/Y
Lannitang Granite						
LN7-2	789	112	−8.14	7.28	0.77	
1	827	87	−7.37	7.14	0.67	
2	856	135	−4.51	9.38	0.72	
3	1001	56	−2.54	8.58	0.54	
4	790	83	−9.2	6.18	0.77	
5	791	43	−11.67	3.69	0.66	
6	798	122	−7.38	7.81	0.86	
7	784	94	−9	6.52	0.61	
8	792	28	−13.22	2.11	0.69	
9	758	116	−9.49	6.7	0.95	
LN1401	764	30	−14.26	1.75	0.72	
1	788	62	−10.42	5.01	0.75	
2	829	108	−6.48	7.99	0.74	
3	743	52	−13.22	3.33	0.64	
4	754	43	−13.41	2.88	0.73	
5	797	65	−9.8	5.4	0.89	
6	972	39	−4.87	6.75	0.95	
7	814	22	−13.12	1.68	0.67	
8	741	84	−11.51	5.1	0.61	
9	608	83	−19.32	1.37	0.99	

Notes: 1 Temperatures were calculated with a Ti-in-zircon thermometer [37]. 2 Oxygen fugacities were calculated by the method proposed by [34]. 3  $Eu_N/Eu_N^* = Eu_N/\text{SQRT}(Sm_N \cdot Gd_N)$ , where subscript N refers to Chondrite normalized with the data of Sun and McDonough [48]. 4 Trace elements data from [5] for Pulang complex and Yu et al. [75] for Lannitang granite.

## References

- Deng, J.; Wang, Q.F.; Li, G.J.; Li, C.S.; Wang, C.M. Tethys tectonic evolution and its bearing on the distribution of important mineral deposits in the Sanjiang region, SW China. *Gondwana Res.* **2017**, *26*, 419–437. [\[CrossRef\]](#)
- Roger, F.; Jolivet, M.; Malavieille, J. The tectonic evolution of the Songpan–Garzê (North Tibet) and adjacent areas from Proterozoic to Present: A synthesis. *J. Asian Earth Sci.* **2010**, *39*, 254–269. [\[CrossRef\]](#)
- Wang, P.; Dong, G.C.; Santosh, M.; Li, X.F.; Dong, M.L. Triassic ore-bearing and barren porphyries in the Zhongdian arc of SW China: Implications for the subduction of the Paleo-Tethys Ocean. *Int. Geol. Rev.* **2017**, *59*, 1490–1505. [\[CrossRef\]](#)
- Wang, P.; Dong, G.C.; Dong, M.L.; Li, Y.P.; Xu, Y.M.; Pan, Y.N.; Chen, W.; Wu, Z.C. Magma mixing of the Cuojiaoma batholith in the Yidun Arc: Evidence from mafic microgranular enclaves. *Acta Petrol. Sin.* **2017**, *33*, 2535–2547.
- Meng, X.Y.; Mao, J.W.; Zhang, C.Q.; Zhang, D.Y.; Liu, H. Melt recharge,  $fO_2$ -T conditions, and metal fertility of felsic magmas: Zircon trace element chemistry of Cu-Au porphyries in the Sanjiang orogenic belt, southwest China. *Miner. Depos.* **2018**, *53*, 649–663. [\[CrossRef\]](#)
- Wang, P.; Dong, G.C.; Zhao, G.C. Petrogenesis of the Pulang Porphyry Complex, Southwestern China: Implications for Porphyry Copper Metallogeny and Subduction of the Paleo-Tethys Oceanic Lithosphere. *Lithos* **2018**, *304–307*, 280–297. [\[CrossRef\]](#)
- Gao, X.; Yang, L.Q.; Evan, A.O. The lithospheric architecture of two subterranean in the eastern Yidun Terrane, East Tethys: Insights from Hf–Nd isotopic mapping. *Gondwana Res.* **2018**, *62*, 127–143. [\[CrossRef\]](#)
- Zhang, X.; Wang, J. Zircon U–Pb dating and geochemistry of the Changdagou pluton in northwestern Sichuan Province. *Acta Mineral. Sin.* **2015**, *35*, 745–746. (In Chinese with English abstract)
- Blevin, P.L. Redox and compositional parameters for interpreting the granitoid metallogeny of eastern Australia: Implications for gold-rich ore systems. *Resour. Geol.* **2004**, *54*, 241–252. [\[CrossRef\]](#)
- Annen, C.; Blundy, J.; Sparks, R. The genesis of intermediate and silicic magmas in deep crustal hot zones. *J. Petrol.* **2006**, *47*, 505–539. [\[CrossRef\]](#)

11. Loucks, R.R. Distinctive composition of copper-ore-forming arc magmas: Australian. *J. Earth Sci.* **2014**, *61*, 5–16.
12. Dilles, J.H.; Kent, A.J.; Wooden, J.L.; Tosdal, R.M.; Koleszar, A.; Lee, R.G.; Farmer, L.P. Zircon compositional evidence for sulfur-degassing from ore-forming arc magmas. *Econ. Geol.* **2015**, *110*, 241–251. [[CrossRef](#)]
13. Ding, T.; Ma, D.S.; Lu, J.J.; Zhang, R.Q. Apatite in granitoids related to polymetallic mineral deposits in southeastern Hunan Province, Shi-Hang zone, China: Implications for petrogenesis and metallogenesis. *Ore Geol. Rev.* **2015**, *69*, 104–117. [[CrossRef](#)]
14. Lu, Y.J.; Loucks, R.R.; Fiorentini, M.; Mccuaig, T.C.; Evans, N.J.; Yang, Z.M.; Hou, Z.Q.; Kirkland, C.L.; Parra-Avila, L.A.; Kobussen, A.; et al. Chapter 13 Zircon Compositions as a Pathfinder for Porphyry Cu ± Mo ± Au Deposits. *Econ. Geol.* **2016**, *19*, 329–347.
15. Ballard, J.R.; Palin, M.J.; Campbell, I.H. Relative oxidation states of magmas inferred from Ce (IV)/Ce (III) in zircon: Application to porphyry copper deposits of northern Chile. *Contrib. Mineral. Petrol.* **2002**, *144*, 347–364. [[CrossRef](#)]
16. He, D.F.; Zhu, W.G.; Zhong, H.; Ren, T.; Bai, Z.J.; Fan, H.P. Zircon U-Pb geochronology and elemental and Sr-Nd-Hf isotopic geochemistry of the Daocheng granitic pluton from the Yidun Arc, SW China. *J. Asian Earth Sci.* **2013**, *67–68*, 1–17. [[CrossRef](#)]
17. He, M.; Zheng, H.; Clift, P.D. Zircon U-Pb geochronology and Hf isotope data from the Yangtze River sands: Implications for major magmatic events and crustal evolution in Central China. *Chem. Geol.* **2013**, *360–361*, 186–203. [[CrossRef](#)]
18. Guitreau, M.; Blichert-Toft, J.; Martin, H.; Mojzsis, S.J.; Albarède, F. Hafnium isotope evidence from Archean granitic rocks for deep-mantle origin of continental crust. *Earth Planet. Sci. Lett.* **2012**, *337–338*, 211–223. [[CrossRef](#)]
19. Li, W.C.; Zeng, P.S.; Hou, Z.Q.; Noel, C.W. The Pulang porphyry copper deposit and associated felsic intrusions in Yunnan Province, Southwest China. *Econ. Geol.* **2011**, *106*, 79–92.
20. Hu, R.Z.; Zhou, M.F. Multiple Mesozoic mineralization events in South China—An introduction to the thematic issue. *Miner. Depos.* **2012**, *47*, 579–588. [[CrossRef](#)]
21. Xiao, L.; He, Q.; Pirajno, F.; Ni, P.; Du, J.X.; Wei, Q.R. Possible correlation between a mantle plume and the evolution of Paleo-Tethys Jinshajiang Ocean: Evidence from a volcanic rifted margin in the Xiaru-Tuoding area, Yunnan, SW China. *Lithos* **2008**, *100*, 112–126. [[CrossRef](#)]
22. Song, H.; Zhang, C.J.; Li, Y.G.; Zhong, W.L.; Li, J.Q. Geochemical constraints of trace elements on ore-forming fluids in the copper polymetallic deposits in the middle Sanjiang Belts. *Acta Petrol. Sin.* **2016**, *32*, 804–814. (In Chinese with English abstract).
23. Peng, T.; Zhao, G.; Fan, W.; Peng, B.; Mao, Y. Zircon geochronology and Hf isotopes of Mesozoic intrusive rocks from the Yidun terrane, Eastern Tibetan Plateau: Petrogenesis and their bearings with Cu mineralization. *J. Asian Earth Sci.* **2014**, *80*, 18–33. [[CrossRef](#)]
24. Leng, C.B.; Zhang, X.C.; Hu, R.Z.; Wang, S.X.; Zhong, H.; Wang, W.Q.; Bi, X.W. Zircon U-Pb and molybdenite Re-Os geochronology and Sr-Nd-Pb-Hf isotopic constraints on the genesis of the Xuejiping porphyry copper deposit in Zhongdian, Northwest Yunnan, China. *J. Asian Earth Sci.* **2012**, *60*, 31–48. [[CrossRef](#)]
25. Leng, C.B.; Huang, Q.Y.; Zhang, X.C.; Wang, S.C.; Zhong, H.; Hu, R.Z.; Bi, X.W.; Zhu, J.J.; Wang, X.S. Petrogenesis of the Late Triassic volcanic rocks in the Southern Yidun arc, SW China: Constraints from the geochronology, geochemistry and Sr-Nd-Pb-Hf isotopes. *Lithos* **2014**, *190–191*, 363–382. [[CrossRef](#)]
26. Zong, K.Q.; Klemd, R.; Yuan, Y.; He, Z.Y.; Guo, J.L.; Shi, X.L.; Liu, Y.S.; Hu, Z.C.; Zhang, Z.M. The assembly of Rodinia: The correlation of early Neoproterozoic (ca. 900 Ma) high-grade metamorphism and continental arc formation in the southern Beishan Orogen, southern Central Asian Orogenic Belt (CAOB). *Precambrian Res.* **2017**, *290*, 32–48. [[CrossRef](#)]
27. Hu, Z.C.; Zhang, W.; Liu, Y.S.; Gao, S.; Li, M.; Zong, K.Q.; Chen, H.H.; Hu, S.H. “Wave” signal smoothing and mercury removing device for laser ablation quadrupole and multiple collector ICP-MS analysis: Application to lead isotope analysis. *Anal. Chem.* **2015**, *87*, 1152–1157. [[CrossRef](#)]
28. Liu, Y.S.; Gao, S.; Hu, Z.C.; Gao, C.G.; Zong, K.Q.; Wang, D.B. Continental and oceanic crust recycling-induced melt-peridotite interactions in the Trans-North China Orogen: U-Pb dating, Hf isotopes and trace elements in zircons of mantle xenoliths. *J. Petrol.* **2010**, *51*, 537–571. [[CrossRef](#)]

29. Liu, Y.S.; Hu, Z.C.; Gao, S.; Günther, D.; Xu, J.; Gao, C.G.; Chen, H.H. In situ analysis of major and trace elements of anhydrous minerals by LA-ICP-MS without applying an internal standard. *Chem. Geol.* **2008**, *257*, 34–43. [[CrossRef](#)]
30. Ludwig, K.R. *ISOPLLOT 3.00: A Geochronological Toolkit for Microsoft Excel*; Berkeley Geochronology Center: Berkeley, CA, USA, 2003.
31. Woodhead, J.D.; Hergt, J.M.; Shelley, M.; Eggins, S.; Kemp, R. Zircon Hf-isotope analysis with an excimer laser, depth profiling, ablation of complex geometries, and concomitant age estimation. *Chem. Geol.* **2004**, *209*, 121–135. [[CrossRef](#)]
32. Fisher, C.M.; Vervoort, J.D.; Hanchar, J.M. Guidelines for reporting zircon Hf isotopic data by LA-MC-ICPMS and potential pitfalls in the interpretation of these data. *Chem. Geol.* **2014**, *363*, 125–133. [[CrossRef](#)]
33. Blichert-Toft, J.; Chauvel, C.; Albarede, F. Separation of Hf and Lu for high-precision isotope analysis of rock samples by magnetic sector-multiple collector ICP-MS. *Contrib. Mineral. Petrol.* **1997**, *127*, 248–260. [[CrossRef](#)]
34. Trail, D.; Watson, E.B.; Tailby, N.D. Ce and Eu anomalies in zircon as proxies for the oxidation state of magmas. *Geochim. Cosmochim. Acta* **2012**, *97*, 70–87. [[CrossRef](#)]
35. Smythe, D.J.; Brenan, J.M. Cerium oxidation state in silicate melts: Combined  $fO_2$ , temperature and compositional effects. *Geochim. Cosmochim. Acta* **2015**, *170*, 173–187. [[CrossRef](#)]
36. Smythe, D.J.; Brenan, J.M. Magmatic oxygen fugacity estimated using zircon melt partitioning of cerium. *Earth Planet. Sci. Lett.* **2016**, *453*, 260–266. [[CrossRef](#)]
37. Ferry, J.M.; Watson, E.B. New thermodynamic models and revised calibrations for the Ti-in-zircon and Zr-in-rutile thermometers. *Contrib. Mineral. Petrol.* **2007**, *154*, 429–437. [[CrossRef](#)]
38. Qiu, J.T.; Yu, X.Q.; Santosh, M.; Zhang, D.H.; Chen, S.Q.; Li, P.J. Geochronology and magmatic oxygen fugacity of the Tongcun molybdenum deposit, northwest Zhejiang, SE China. *Miner. Depos.* **2013**, *48*, 545–556. [[CrossRef](#)]
39. Qiu, J.T.; Yu, X.Q.; Santosh, M.; Li, P.J.; Zhang, D.H.; Xiong, G.Q.; Zhang, B.Y. The Late Mesozoic tectonic evolution and magmatic history of west Zhejiang, SE China: Implications for regional metallogeny. *Int. J. Earth Sci.* **2014**, *103*, 713–735. [[CrossRef](#)]
40. Loader, M.A.; Wilkinson, J.J.; Armstrong, R.N. The effect of titanite crystallization on Eu and Ce anomalies in zircon and its implications for the assessment of porphyry Cu deposit fertility. *Earth Planet. Sci. Lett.* **2017**, *472*, 107–119. [[CrossRef](#)]
41. Thomas, R. Determination of water contents of granite melt inclusions by confocal laser Raman microprobe spectroscopy. *Am. Mineral.* **2000**, *85*, 868–872. [[CrossRef](#)]
42. Thomas, R.; Davidson, P. Water in granite and pegmatite-forming melts. *Ore Geol. Rev.* **2012**, *46*, 32–46. [[CrossRef](#)]
43. Williamson, B.J.; Herrington, R.J.; Morris, A. Porphyry copper enrichment linked to excess aluminum in plagioclase. *Nat. Geosci.* **2015**, *9*, 237–241.
44. Burnham, C.W. Water and magmas; A mixing model. *Geochim. Cosmochim. Acta* **1975**, *39*, 1077–1084. [[CrossRef](#)]
45. Liang, H.Y.; Sun, W.D.; Su, W.C.; Zartman, R.E. Porphyry copper-gold mineralization at Yulong, China, promoted by decreasing redox potential during magnetite alteration. *Econ. Geol.* **2009**, *104*, 587–596. [[CrossRef](#)]
46. Zhang, W.; Lentz, D.R.; Thorne, K.G.; McFarlane, C. Geochemical characteristics of biotite from felsic intrusive rocks around the Sisson Brook W–Mo–Cu deposit, west-central New Brunswick: An indicator of halogen and oxygen fugacity of magmatic systems. *Ore Geol. Rev.* **2016**, *77*, 82–96. [[CrossRef](#)]
47. Zhang, J.R.; Li, X.Y.; Ye, M. Research progress on Ce anomaly method for calculating oxygen fugacity of granite and applicability. *Chin. Rare Earths* **2018**, *39*, 20–27. (In Chinese with English abstract)
48. Belousova, E.A.; Griffin, W.L.; Reilly, S.Y. Igneous zircon: Trace element composition as an indicator of source rock type. *Contrib. Mineral. Petrol.* **2002**, *143*, 602–622. [[CrossRef](#)]
49. Hoskin, P.W.O.; Schaltegger, U. The composition of zircon and igneous and metamorphic petrogenesis. *Rev. Miner. Geochem.* **2003**, *53*, 27–62. [[CrossRef](#)]
50. Zeng, Y.F. The Geological Characteristics and Discussions on the Genesis of Porphyry Copper Deposit in Changdagou. Master's Thesis, Chengdu University of Technology, Chengdu, China, 2015; 62p. (In Chinese with English abstract)

51. Blichert-Toft, J.; Albarede, F. The Lu–Hf isotope geochemistry of chondrites and the evolution of the mantle–crust system. *Earth Planet. Sci. Lett.* **1997**, *148*, 243–258. [[CrossRef](#)]
52. Griffin, W.L.; Pearson, N.J.; Belousova, E.; Jackson, S.E.; van Achterbergh, E.; O'Reilly, S.Y.; Shee, S.R. The Hf isotope composition of cratonic mantle: LAM-MC-ICPMS analysis of zircon megacrysts in kimberlites. *Geochim. Cosmochim. Acta* **2000**, *64*, 133–147. [[CrossRef](#)]
53. Li, S.R.; Yang, X.G.; Cheng, D.G.; Guo, P. Metallogenic regularity and prospecting potential of manganese deposits in Sichuan. *Acta Geol. Sichuan* **2012**, *32*, 21–25, (In Chinese with English abstract).
54. Chen, J.L.; Xu, J.F.; Ren, J.B.; Huang, X.X.; Wang, B.D. Geochronology and geochemical characteristics of late Triassic porphyritic rocks from the Zhongdian arc, eastern Tibet, and their tectonic and metallogenic implications. *Gondwana Res.* **2014**, *26*, 492–504. [[CrossRef](#)]
55. Ren, J.B.; Xu, J.F.; Chen, J.L. Zircon geochronology and geological implications of ore-bearing porphyries from Zhongdian arc. *Acta Petrol. Sin.* **2011**, *27*, 2591–2599, (In Chinese with English abstract).
56. Reid, A.J.; Wilson, C.J.L.; Liu, S. Structural evidence for the Permo-Triassic tectonic evolution of the Yidun Arc, eastern Tibetan Plateau. *J. Struct. Geol.* **2005**, *27*, 119–137. [[CrossRef](#)]
57. Reid, A.J.; Wilson, C.J.L.; Shun, L.; Pearson, N.; Belousova, E. Mesozoic plutons of the Yidun Arc, SW China: U/Pb geochronology and Hf isotopic signature. *Ore Geol. Rev.* **2007**, *31*, 88–106. [[CrossRef](#)]
58. Shen, P.; Hattori, K.; Pan, H.; Jackson, S.; Seitmuratova, E. Oxidation condition and metal fertility of granitic magmas: Zircon trace-element data from porphyry Cu deposits in the Central Asian Orogenic Belt. *Econ. Geol.* **2015**, *110*, 1861–1878. [[CrossRef](#)]
59. Sun, W.D.; Liang, H.Y.; Ling, M.X.; Zhan, M.Z.; Ding, X.; Zhang, H.; Yang, X.Y.; Li, Y.L.; Ireland, T.R.; Wei, Q.R. The link between reduced porphyry copper deposits and oxidized magmas. *Geochim. Cosmochim. Acta* **2013**, *103*, 263–275. [[CrossRef](#)]
60. Sun, W.D.; Huang, R.F.; Li, H.; Hu, Y.B.; Zhang, C.C.; Sun, S.J.; Zhang, L.P.; Ding, X.; Li, C.Y.; Zartman, R.E. Porphyry deposits and oxidized magmas. *Ore Geol. Rev.* **2015**, *65*, 97–131. [[CrossRef](#)]
61. Jugo, P.; Candela, P.; Piccoli, P. Magmatic sulfides and Au: Cu ratios in porphyry deposits: An experimental study of copper and gold partitioning at 850 °C, 100 MPa in a haplogranitic melt–pyrrhotite–intermediate solid solution–gold metal assemblage, at gas saturation. *Lithos* **1999**, *46*, 573–589. [[CrossRef](#)]
62. Mungall, J.E. Roasting the mantle: Slab melting and the genesis of major Au and Au-rich Cu deposits. *Geology* **2002**, *30*, 915–918. [[CrossRef](#)]
63. Mungall, J.E.; Brenan, J.M. Partitioning of platinum-group elements and Au between sulfide liquid and basalt and the origins of mantle–crust fractionation of the chalcophile. *Chem. Geol.* **2014**, *120*, 223–253. [[CrossRef](#)]
64. Nicholls, J. A simple thermodynamic model for estimating the solubility of H<sub>2</sub>O in magmas. *Contrib. Mineral. Petrol.* **1980**, *74*, 211–220. [[CrossRef](#)]
65. Sillitoe, R.H. Porphyry copper systems. *Econ. Geol.* **2010**, *105*, 3–41. [[CrossRef](#)]
66. Wang, R.; Richards, J.P.; Hou, Z.-Q.; Yang, Z.-M.; Gou, Z.-B.; DuFrane, S.A. Increasing magmatic oxidation state from Paleocene to Miocene in the eastern Gangdese Belt, Tibet: Implication for collision-related porphyry Cu–Mo ± Au mineralization. *Econ. Geol.* **2014**, *109*, 1943–1965. [[CrossRef](#)]
67. Wang, R.; Richards, J.P.; Hou, Z.; Yang, Z.; DuFrane, S.A. Increased Magmatic Water Content—The Key to Oligo-Miocene Porphyry Cu–Mo ± Au Formation in the Eastern Gangdese Belt, Tibet. *Econ. Geol.* **2014**, *109*, 1315–1339. [[CrossRef](#)]
68. Wang, F.Y.; Ling, M.X.; Ding, X.; Hu, Y.H.; Zhou, J.B.; Yang, X.Y.; Liang, H.Y.; Fan, W.M.; Sun, W. Mesozoic large magmatic events and mineralization in SE China: Oblique subduction of the Pacific plate. *Int. Geol. Rev.* **2011**, *53*, 704–726. [[CrossRef](#)]
69. Yavuz, F. Evaluating micas in petrologic and metallogenic aspect: I—Definitions and structure of the computer program MICA+. *Comput. Geosci.* **2003**, *29*, 1203–1213. [[CrossRef](#)]
70. Yavuz, F. Evaluating micas in petrologic and metallogenic aspect: Part II—Applications using the computer program Mica+. *Comput. Geosci.* **2003**, *29*, 1215–1228. [[CrossRef](#)]
71. Richards, J.P. The oxidation state, and sulfur and Cu contents of arc magmas: Implications for metallogeny. *Lithos* **2015**, *233*, 27–45. [[CrossRef](#)]
72. Cai, H.M.; Zhang, H.F.; Xu, W.C.; Shi, Z.L.; Yuan, H.L. Petrogenesis of Indosinian volcanic rocks in Songpan-Garze fold belt of the northeastern Tibetan Plateau: New evidence for lithospheric delamination. *China Earth Sci.* **2010**, *53*, 1316–1328. [[CrossRef](#)]

73. Hou, Z.Q.; Gao, Y.F.; Qu, X.M.; Rui, Z.Y.; Mo, X.X. Origin of adakitic intrusions generated during mid-Miocene east-west extension in southern Tibet. *Earth Planet. Sci. Lett.* **2004**, *220*, 139–155. [[CrossRef](#)]
74. Hou, Z.Q.; Zheng, Y.C.; Yang, Z.M.; Rui, Z.Y.; Zhao, Z.D.; Jiang, S.H.; Qu, X.M.; Sun, Q.Z. Contribution of mantle components within juvenile lower-crust to collisional zone porphyry Cu systems in Tibet. *Miner. Depos.* **2013**, *48*, 173–192. [[CrossRef](#)]
75. Yu, Y.F.; Fei, G.C.; Li, Y.G.; Long, X.R.; Tian, E.Y.; Liu, G.Q.; Lv, F.M.; Hua, K.Q. Oxygen Fugacity Characteristics and Metallogenic Significance of Porphyry Copper Deposit in Zhongdian Island. *Chin. Rare Earths* **2018**, *39*, 20–27. (In Chinese with English abstract)



© 2019 by the authors. Licensee MDPI, Basel, Switzerland. This article is an open access article distributed under the terms and conditions of the Creative Commons Attribution (CC BY) license (<http://creativecommons.org/licenses/by/4.0/>).